PNAS RESEARCH ARTICLE | APPLIED BIOLOGICAL SCIENCES

Engineered bacteria that self-assemble bioglass polysilicate coatings display enhanced light focusing

Lynn M. Sidor[a], Michelle M. Beaulieu[b], Ilia Rasskazov[c,1], B. Cansu Acarturk[d], Jie Ren[d], Emerson Jenen[a], Lycka Kamoen[e,2], María Vázquez Vitali[e], P. Scott Carney[c], Greg R. Schmidt[c], Wil V. Srubar III[d,f], Elio A. Abbondanzieri[a], and Anne S. Meyer[a,3]

Affiliations are included on p. 11.

Edited by Steven Block, Stanford University, Stanford, CA; received May 9, 2024; accepted October 17, 2024

Cutting-edge photonic devices frequently rely on microparticle components to focus and manipulate light. Conventional methods used to produce these microparticle components frequently offer limited control of their structural properties or require low-throughput nanofabrication of more complex structures. Here, we employ a synthetic biology approach to produce environmentally friendly, living microlenses with tunable structural properties. We engineered *Escherichia coli* bacteria to display the silica biomineralization enzyme silicatein from aquatic sea sponges. Our silicatein-expressing bacteria can self-assemble a shell of polysilicate "bioglass" around themselves. Remarkably, the polysilicate-encapsulated bacteria can focus light into intense nanojets that are nearly an order of magnitude brighter than unmodified bacteria. Polysilicate-encapsulated bacteria are metabolically active for up to 4 mo, potentially allowing them to sense and respond to stimuli over time. Our data demonstrate that synthetic biology offers a pathway for producing inexpensive and durable photonic components that exhibit unique optical properties.

synthetic biology | bioglass | engineered living materials | silicatein | photonic nanojets

Significance

In this work, we apply the principles of synthetic biology to create living optical devices. Utilizing the ability of sea sponges to polymerize bioglass from silica precursors in the ocean water using only a single enzyme, silicatein, we have fused this same enzyme to the surface of *Escherichia coli* bacterial cells. The modified bacteria can polymerize a layer of bioglass at their surface. This bioglass shell allows the bacteria to act as engineered optical devices that are able to scatter high intensity, focused light while also surviving for several months, opening the door to a wide range of sense-and-respond applications.

In nature, organisms have evolved innate abilities to produce multifunctional structures with complex compositions and advanced optical properties. These biologically produced structures have vast potential to be used to design and produce optical materials and devices using ecologically friendly manufacturing methods. In particular, certain biological structures show great promise as next-generation microlenses and optical microparticles. Microscopic organisms, cells, and materials produced by living organisms have already been shown to exhibit unique and beneficial properties for manipulating light. These "biomicrolenses" have been demonstrated to act as superresolution magnifiers (1), to enhance upconversion in fluorescence (2), to sense light direction (3), to enable subdiffractive focusing (4), and to act as waveguides (5).

In addition, cell-based biomicrolenses are similar in size and shape to photonic structures that are used for subwavelength microscopy and the formation of photonic nanojets (6–11). Nanojets are narrow, intense electromagnetic beams (9) that form behind microlenses and other microparticles when illuminated by light with a wavelength near the size of the particle. This phenomenon resembles a lensing effect but cannot be modeled by refraction alone, since interference and scattering effects significantly affect the shape of the beam of light. Control of parameters such as size, shape, and index of refraction of the microsphere "lens" can be used to engineer the shape of the nanojet, which can take forms ranging from submicron, high-intensity spots to multimicron, medium-intensity beams (12). However, in order to tailor biological particles to specific applications, we need the ability to tune their optical properties.

Synthetic biology offers a path to engineer single cells by altering their size, length, shape, and refractive index, all of which can be used to optimize their ability to act as biophotonic microlenses. Synthetic biology approaches can also be used to combine unique optical functions of different organisms. Many aquatic organisms, including sea stars and sponges, possess the ability to synthesize natural structures that perform both optical and structural functions. The arms of the brittlestar are coated in light-sensitive calcite plates, which provide protection and also act as highly efficient light-capturing microlens arrays (13, 14). Similarly, hexactinellid sponges create silica spicules that are responsible for their structural stability and also display waveguide properties (15, 16). Siliceous sponges deposit silica into needle-like spicules, which is accomplished by polymerizing silica into polysilicate, also known as "bioglass," using a unique silicatein enzyme (17–21). Silicatein-catalyzed silica deposition requires only a single gene to be expressed and can be performed at physiological temperature, pressure, and pH without the use of harsh or toxic chemicals

Author contributions: L.M.S., M.M.B., I.R., L.K., M.V.V., E.A.A., and A.S.M. designed research; L.M.S., M.M.B., I.R., B.C.A., J.R., E.J., L.K., M.V.V., E.A.A., and A.S.M. performed research; L.M.S., M.M.B., I.R., E.A.A., and A.S.M. contributed new reagents/analytic tools; L.M.S., M.M.B., I.R., B.C.A., J.R., E.J., P.S.C., G.R.S., W.V.S., E.A.A., and A.S.M. analyzed data; and L.M.S., M.M.B., I.R., B.C.A., J.R., L.K., M.V.V., P.S.C., G.R.S., W.V.S., E.A.A., and A.S.M. wrote the paper.

Competing interest statement: L.M.S. and A.S.M. Modified bacteria and methods of use for bioglass microlenses. Provisional US patent application No. 63/338,490, filed May 5, 2022. International Patent Cooperation Treaty patent application filed May 5, 2023.

This article is a PNAS Direct Submission.

[1] Present address: SunDensity Inc., Rochester, NY 14604.

[2] Present address: Institute of Biology, Leiden University, Leiden 2333 BE, The Netherlands.

[3] To whom correspondence may be addressed. Email: anne.meyer@rochester.edu.

This article contains supporting information online at https://www.pnas.org/lookup/suppl/doi:10.1073/pnas.2409335121/-/DCSupplemental.

(22, 23). Silicatein is thought to be the only natural biomineralizing enzyme (24), and its ability to fabricate polysilicate structures offers a powerful addition to the synthetic biology toolbox.

In this article, we use multiphysics modeling to demonstrate that polysilicate-encapsulated bacterial cells are predicted to have enhanced abilities to scatter and focus light into photonic nanojets. We then demonstrate that engineered *Escherichia coli* bacteria that express surface-displayed silicatein enzymes from sea sponges *Tethya aurantia* and *Suberites domuncula* can coat themselves in a layer of polysilicate. We observe that these cells scatter and focus light in a manner that resembles the modeled data. Using a fluorescent probe, we show that the polysilicate-encapsulated bacterial cells, when exposed to planar illumination, create intense beams of focused light that form a peak of intensity outside the cell. In contrast, wild-type bacteria create much weaker beams that peak at the cell surface. Remarkably, polysilicate-encapsulated cells survive for up to 4 mo postencapsulation and are still able to scatter light with a comparable focal peak after they become metabolically inactive. These optically tuned bacteria represent biologically engineered microlenses, and they have the potential to create biologically active devices with controllable properties for optimizing optical performance across a variety of applications including advanced biosensing, superresolution imaging, Raman scattering, nanolithography, and photovoltaics (3, 4).

Results

Prediction of Enhanced Nanojets. We first set out to test whether a thin polysilicate shell would be expected to have a measurable impact on the ability of a bacterial cell to focus light. We therefore simulated the passage of light through a typically sized *E. coli* bacterial cell surrounded by a uniform coating of polysilicate using the finite-difference time domain (FDTD) method (*SI Appendix*, Fig. S1 *A* and *B*), a method that has previously been used to model photonic nanojets and microspheres (25, 26). The electric field intensity throughout the simulation region is a superposition of incident and scattered light (27), allowing us to create intensity maps showing the brightness of the light in the vicinity of the bacterial cells (Fig. 1 *A* and *B*). At an angle of incidence of 0°, i.e. with the long axis of the cells aligned in the same direction as the light, the intensity maps demonstrated that the encapsulated cells produced a bright central beam of scattered light, as well as less-intense peripheral beams (Fig. 1*A*). Wild-type cells were modeled identically to the encapsulated cells but without a polysilicate coating, and the intensity maps of the wild-type cells showed a beam that was less intense compared to the encapsulated cells (Fig. 1*B*).

Simulations were next performed for bacterial cells at a range of angles relative to the incident light, to capture the scattering patterns that might be observed from cells deposited on a surface in random orientations. For both wild-type and polysilicate-coated simulated cells, the intensity was calculated for cell angles between 0° to 90° at 5° or 10° increments. The angle of the cells was varied rather than the angle of the incident light to ensure that the amount of light entering the simulation region remained constant across simulations, as well as to maintain a roughly consistent position and direction of the scattered beam within the simulation region. We were therefore able to perform the simulations over a consistent volume in space for all incident angles. In order to quantify the length and intensity of the central scattered beam, we determined the boundary where the beam intensity exceeded the background intensity by 30%. This calculation allowed us to define the length and integrated intensity of the scattered beam (Fig. 1 *C* and *D*). Although the polysilicate layer only modestly increased the diameter and average index of refraction of the cells, the scattered beams of light were significantly longer and brighter compared to the modeled wild-type cells. To determine the width of the beam, we calculated the full width at half maximum (FWHM) of the central peak after subtracting the background intensity (Fig. 1*E* and *SI Appendix*, Fig. S1 *C* and *D*). The narrowest beams had widths below 0.4 μm (0.8 λ, where λ is the wavelength of illuminating light). The encapsulated cells produced beams that were focused deeper into solution and were moderately broader (*SI Appendix*, Fig. S1 *E* and *F*). The focal shift due to encapsulation ranged from 0.28 μm deeper at 0° incidence up to 0.49 μm deeper at 90° incidence. The angle of the modeled cells relative to the incoming light was seen to have an effect on both the intensity of the scattered light and the location of the focal peak relative to the bacterial cell, with larger angles resulting in lower-intensity scattered light with a peak farther away from the cell body (Fig. 1 *F* and *G*). Taken together, these modeling data indicate that polysilicate-coated bacterial cells are expected to generate significantly brighter and longer photonic nanojets compared to wild-type bacterial cells.

Construction of Silicatein-Expressing Strains. In order to construct bacterial strains that express silicatein enzymes on the cell surface, where they can interact with silica precursor molecules in solution and biomineralize a layer of polysilicate bioglass, silicatein enzymes from *T. aurantia* or *S. domuncula* sea sponges were fused to a bacterial outer membrane protein [outer membrane protein A (OmpA) (28) or ice nucleation protein (INP) (29)]. Constructs containing INP-*T. aurantia* silicatein were not able to be created either though gene synthesis or traditional restriction enzyme-based assembly. Expression of an INP-*S. domuncula* silicatein construct in *E. coli* resulted in high rates of abnormal cell elongation morphology following the polysilicate encapsulation protocol and showed a varying pattern of polysilicate staining with Rhodamine123. Therefore, INP-silicatein fusions were not used further. To achieve multiple types of induction control, OmpA-silicatein constructs were cloned into several inducible plasmids (pBAD33, pTrc99a, pRHA109, pRHA113, and pBbS5a). Any constructs cloned into pTrc99a were lethal upon induction, and cloning into pRHA109 was repeatedly unsuccessful. OmpA-silicatein constructs cloned into pBAD33 showed two distinct cell populations after induction: cells that demonstrated successful peripheral Rhodamine123 staining and cells that showed low-intensity, homogeneous staining, likely indicative of nonencapsulated cells; these strains were not used further. The *E. coli* strain expressing pBbS5a OmpA-*T. aurantia* silicatein (TaSil) showed consistent peripheral Rhodamine123 staining patterns and normal cell morphology and is used throughout this work. The only pRHA113 construct that was able to be synthesized was OmpA-*S. domuncula* silicatein (SdSil), which is used in this work as well. We attribute the variable success of these constructs to the overexpression of the outer membrane proteins, which can negatively impact cell viability, and the hydrophobicity of the silicatein enzyme.

Silicatein Localizes to Cell Borders. For our constructed strains that expressed OmpA-silicatein fusion proteins, we tested whether the silicatein enzyme was displayed on the surface of the *E. coli* cells after silicatein induction and incubation with orthosilicate, via performing immunofluorescence using an anti-silicatein antibody. Confocal imaging revealed that the immunofluorescence signal was localized to the bacterial cell surface on the cells expressing the OmpA-silicatein constructs (Fig. 2 *A* and *B*). The SdSil-expressing strain showed the localization of the enzyme to broad regions of the cell surface while the TaSil-expressing strain showed more punctate

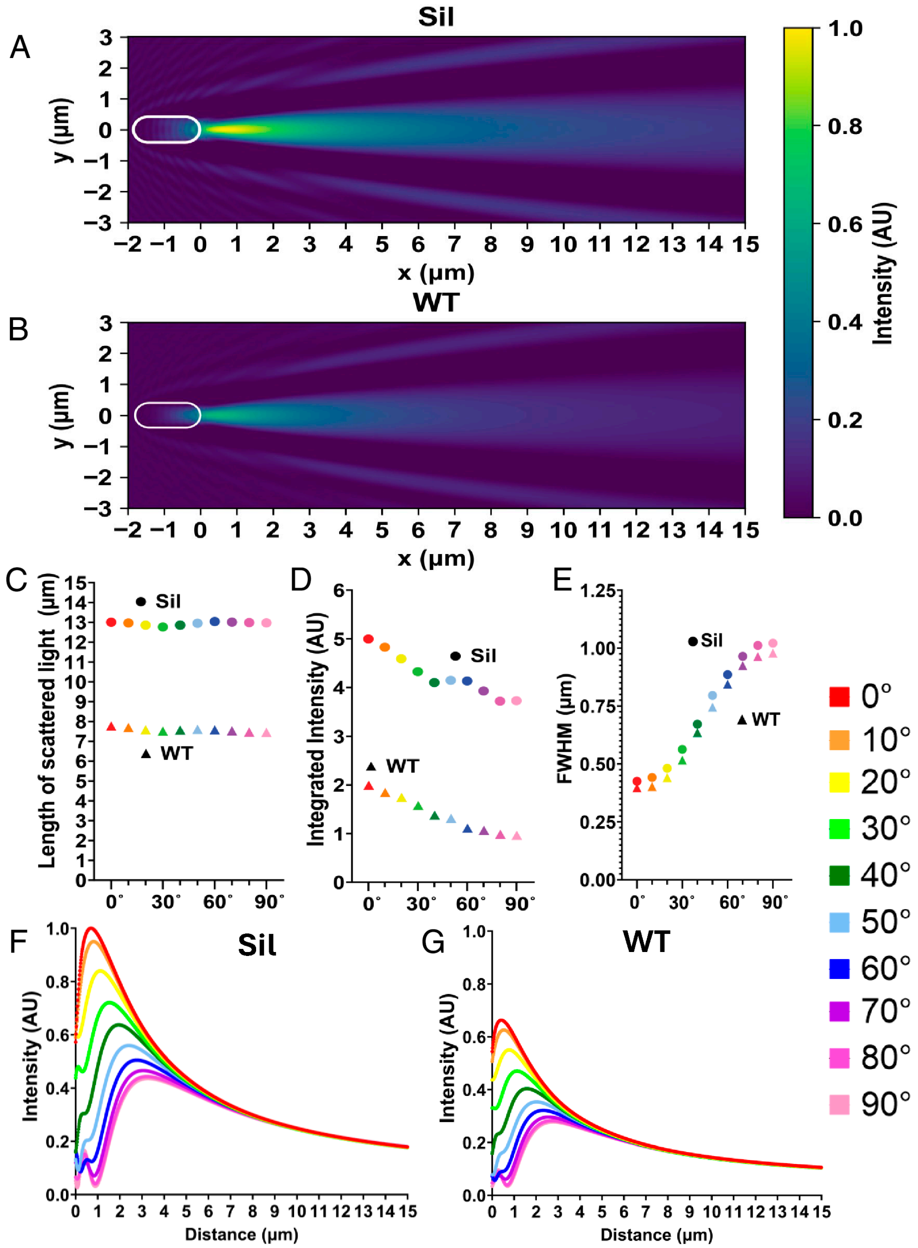

Fig. 1. Mathematical simulations predict that polysilicate-encapsulated bacteria can produce photonic nanojets. (*A* and *B*) Intensity map showing the light scattered by a modeled polysilicate-encapsulated bacteria cell (Sil) (*A*) and a modeled wild-type cell (WT) (*B*). (*C*–*G*) Each color corresponds to a different angle of the cell in relation to the incident light, where (*C*) is the length of scattered light, (*D*) is the normalized integrated intensity of the scattered light, and (*E*) is the FWHM. (*F* and *G*) Normalized intensity of the scattered light as a function of distance from the edge of the cell for different angles of incident light for polysilicate-encapsulated cells (Sil) (*F*) and WT (*G*).

localization. The wild-type cells showed background levels of binding of the anti-silicatein antibody with no specific localization pattern (Fig. 2*C*). Quantification of the immunofluorescence intensities revealed that the silicatein-expressing strains both showed significantly higher immunofluorescence (165.9 AU and 326.4 AU for TaSil and SdSil respectively) than the wild-type control cells (94.73 AU) (Fig. 2*D*). The differences in the immunofluorescence intensities and localization patterns between the TaSil- and the SdSil-expressing cells may be attributable to the fact that the anti-silicatein antibody was raised against spicules from *S. domuncula* sea sponges, which express a version of the silicatein enzyme that is approximately one-third smaller than the TaSil. Immunofluorescence on both the TaSil and SdSil strains after silicatein induction but not incubation with orthosilicate showed comparable antibody binding intensities and spatial distributions to those seen for the same strains incubated with orthosilicate (228.8 AU and 267.9 AU for TaSil and SdSil with no orthosilicate respectively), while the empty vector (EV) control strain showed little-to-no binding (66.07 AU), similar to the wild-type strain (*SI Appendix*, Fig. S2 *A*–*D*). These immunofluorescence results indicate that the engineered strains are able to express and display silicatein enzymes localized to their outer surfaces.

Encapsulation with Polysilicate. To determine whether the silicatein-expressing strains were able to mineralize a layer of polysilicate surrounding the cells, the strains were first grown in liquid culture, induced for 3 h, and then incubated with orthosilicate for 3 h. All these steps were performed in a shaking incubator. Cells were then stained with Rhodamine123 dye, which adsorbs to silicate materials (7, 10). Both of the silicatein-expressing strains showed a bright Rhodamine123 signal localized to the outer border of the cells, while wild-type cells showed dim,

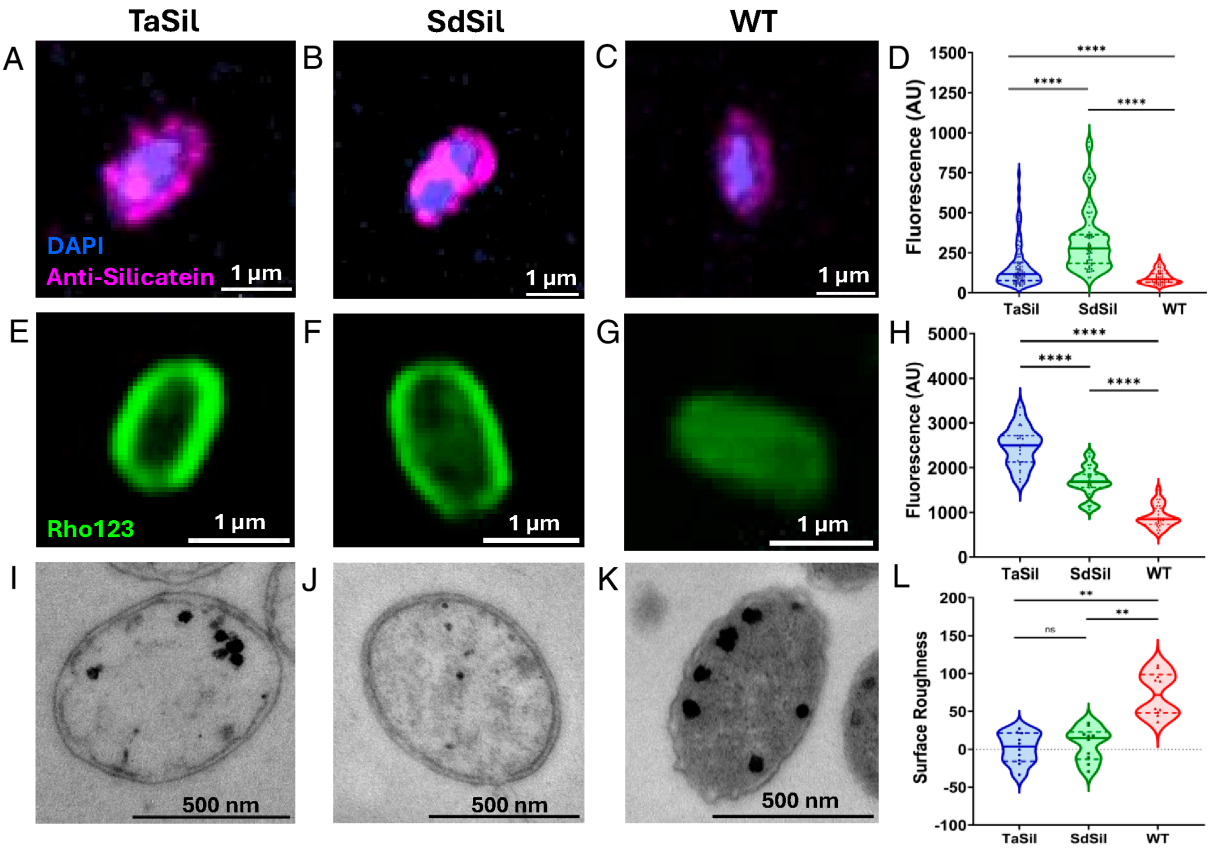

Fig. 2. Silicatein-expressing cells display a smooth polysilicate border. (*A*–*C*) Immunofluorescence of silicatein-expressing (TaSil and SdSil) (*A* and *B*) and WT (*C*) strains following silicatein induction and incubation with orthosilicate. (*D*) Quantification of antibody fluorescence intensity of *A*–*C* ($n_{TaSil} = 90$, $n_{SdSil} = 60$, $n_{WT} = 60$). (*E*–*G*) Rhodamine123 staining of silicatein-expressing (*E* and *F*) and wild-type (*G*) strains. (*H*) Quantification of maximum Rhodamine123 fluorescence signal of *E*–*G* (n = 20). (*I*–*K*) TEM thin section imaging of silicatein-expressing (*I* and *J*) and WT (*K*) strains. (*L*) Quantification of surface roughness of *I*–*K* (n = 10). ****$P \leq 0.0001$, **$P \leq 0.01$, ns: not significant.

diffuse staining (Fig. 2 *E*–*G* and *SI Appendix*, Fig. S3 *A*–*C*). The maximum intensity of the Rhodamine123 signal for individual cells was significantly higher for TaSil and SdSil strains than for wild-type cells (Fig. 2*H*). Quantification of the ratio of the border-to-internal fluorescence signal for Rhodamine123-stained cells indicated that the Rhodamine123 signal was several times higher on the border of the TaSil and SdSil cells than in the interior of the cells (*SI Appendix*, Fig. S3*D*). The border-to-internal ratios of Rhodamine123 fluorescence for the TaSil and SdSil cells were significantly higher than the ratios for the wild-type cells, which showed a ratio close to 1. TaSil and SdSil strains that were induced but not incubated with orthosilicate, as well as the EV control strain, all showed dimmer staining phenotypes (*SI Appendix*, Fig. S4 *A*–*F*) and significantly lower border-to-internal fluorescence ratios (*SI Appendix*, Fig. S4*G*) than the engineered strains that were incubated with orthosilicate. These results indicate that the expression of silicatein enzymes on the outer surfaces of the TaSil and SdSil *E. coli* cells allowed them to encapsulate themselves in a layer of polysilicate coating the outside of the cells.

To determine the longevity of the biomineralized polysilicate coating on the engineered cells, Rhodamine123 staining was repeated on strains that had been stored in buffer for extended periods of time following encapsulation with polysilicate. One-month-old and 5-mo-old encapsulated TaSil and SdSil cells continued to display bright staining on their outer surfaces and had a border-to-internal fluorescence ratio that was significantly higher than for the 1-mo-old and 5-mo-old wild-type cells (*SI Appendix*, Figs. S3*D* and S5 *A*–*C*). The 5-mo cells showed higher border-to-internal fluorescence ratios than cells measured at earlier timepoints (*SI Appendix*, Figs. S3*D* and S5 *D*–*F*), potentially due to increased Rhodamine123 staining in dead or metabolically inactive cells (30). These data indicate that the polysilicate layer surrounding on the engineered cells can be stable for several months following initial biomineralization.

Encapsulated Cells Have Smoother Borders. To determine the cell morphology of the polysilicate-coated cells, transmission electron microscopy (TEM) was performed on thin sections of cells for each strain following silicatein induction and incubation with orthosilicate (Fig. 2 *I*–*K*). The polysilicate-encapsulated cells showed a smooth, nonruffled cell border phenotype, while wild-type cells had a typical ruffled outer membrane phenotype (31). The cell perimeter values of the thin-sectioned cells were determined from the TEM images and used to calculate cell surface roughness values. The polysilicate-coated cells showed significantly smoother cell perimeters than the wild-type cells and empty-vector control cells (Fig. 2*L* and *SI Appendix*, Fig. S6 *A*–*E*). The surface roughnesses of the polysilicate-coated TaSil and SdSil cells were not significantly different from each other (Fig. 2*L* and *SI Appendix*, Fig. S6*E*). Additionally, we observed that the wild-type cells displayed a darker, more electron-dense cell interior than the polysilicate-encapsulated strains. Quantification of the intensities of the cell interiors revealed that the polysilicate-coated strains were significantly less electron-dense than the wild-type cells (*SI Appendix*, Fig. S6*F*). The exact thickness and uniformity of the polysilicate layer was not able to be determined from these images, but we conclude that the thickness does not significantly exceed the thickness of the outer membrane of the *E. coli* cells,

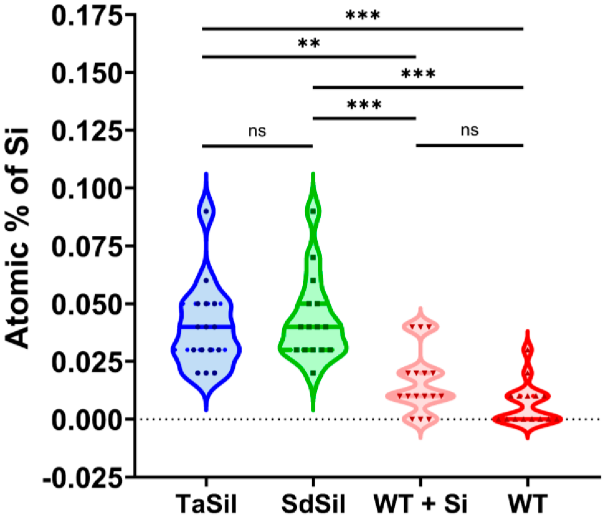

Fig. 3. Silica detection on the surface of silicatein-expressing cells via SEM-EDS. Quantification of the atomic percent of elemental silica from EDS spectra readings of silicatein-expressing strains (TaSil and SdSil) following silicatein induction and incubation with orthosilicate, and the wild-type strain incubated (WT + Si) or not incubated (WT) with orthosilicate (n_{TaSil} = 15, n_{SdSil} = 15, n_{EV} = 13, n_{WT} = 15, $n_{WT+silica}$ = 16). ***P* ≤ 0.01, ****P* ≤ 0.001, ns: not significant.

as the outer-layer thickness did not appear to be different across the strains within our resolution (~7 nm). These analyses indicate that polysilicate coating of the TaSil and SdSil cells results in the formation of a smooth outer cell surface.

Detection of Silica Deposition. To analyze the silica composition on the surface of our silicatein-expressing cells, the strains were induced, incubated with orthosilicate, and analyzed via scanning electron microscopy-energy dispersive X-ray spectroscopy (SEM-EDS). SEM images of the morphology of the cells showed that the silicatein-expressing cells appeared to aggregate in viscous clumps at the high densities used for this experiment, consistent with previous reports (7) (*SI Appendix*, Fig. S7). EDS spectra indicated the presence of silica in the TaSil and SdSil cells, which displayed significantly more silica than the wild-type cells (Fig. 3). Incubation of the wild-type cells with orthosilicate did not result in the detection of a significantly different amount of silica than for wild-type cells without the added orthosilicate, indicating that the levels of silica measured for both wild-type samples represent the background level of detection for this assay. X-ray diffraction (XRD) analysis was also consistent with the presence of silica-containing minerals in our silicatein-expressing, polysilicate-encapsulated strains (*SI Appendix*, Fig. S8).

Increased Scattering Forces Measured on Encapsulated Cells. To analyze whether the polysilicate coating produced detectable effects on the index of refraction of the bacteria, we used optical tweezers to trap individual bacterial cells. A power spectrum analysis (32) demonstrated that the Brownian motion of these bacteria was indistinguishable from that predicted for a sphere of comparable size (*SI Appendix*, Fig. S9*A*). Fitting the power spectra of trapped particles allowed us to extract both a stiffness and effective diameter of each particle (*Materials and Methods*). These two quantities were roughly linearly proportional to each other over this size range, and their ratio depended on the refractive index, as can be seen by a comparison of trapped silica and polystyrene spheres (*SI Appendix*, Fig. S9*B*). Trapped bacteria showed significant variation in their effective length and stiffness, but these quantities were still roughly linearly related (*SI Appendix*, Fig. S9*C*). However, the stiffness to length ratio was noticeably lower for polysilicate-encapsulated bacteria compared to wild-type cells (*SI Appendix*, Fig. S9*D*). Given that the polysilicate coating is relatively thin, we assume that the primary effect of the high-index-of-refraction coating will be to increase the scattering force, pushing the bacteria farther from the beam waist and decreasing the trapping efficiency (33), consistent with the observed results.

Polysilicate-Coated Cells Can Generate Photonic Nanojets. To determine the ability of our polysilicate-encapsulated cells to scatter and focus light, we used a custom-built microscope (*SI Appendix*, Fig. S10) capable of illuminating the bacteria at incident angles ranging from −90° to 90°, a technique we term Multiple Angle Illumination Microscopy (MAIM). By adjusting the position of the illuminating beam at the back focal plane of a 1.49 NA oil-immersion objective (Fig. 4*A*), we could continuously vary the illumination from vertical (i.e., epi-illumination) to horizontal before the beam is cut off by total internal reflection. Cells were vortexed and pipetted thoroughly to break up any clumps and then mounted under an agarose pad. The liquid and agarose around the cells contained the fluorescent dye Alexa-488, allowing us to directly visualize the size and shape of the scattered light above the coverslip. We continually recorded the fluorescence around the bacteria as the illumination angle was varied from −90° to +90°.

The polysilicate-encapsulated cells were seen to scatter a bright jet of light that was most visible at near-horizontal illumination and showed close agreement with the scattering patterns that were predicted to be imaged by multiscale modeling (*SI Appendix*, Fig. S11). To ensure that each cell was exposed to the same set of illumination conditions, we recorded the scattered light across the full range of illumination angles (Movies S1–S3) and created a maximum intensity projection across the sequence (Fig. 4*B*). Wild-type cells occasionally produced diffuse, dimmer jets of scattered light, but most wild-type cells did not scatter a measurable jet of light (Fig. 4*B*). Using the maximum intensity projections, the boundary of the jet was defined as a contiguous region downstream of the bacterial cells for which the fluorescence intensity values were greater than the background intensity value. The jets of light scattered by the encapsulated cells were significantly longer and wider than the light scattered by the wild-type cells (Fig. 4 *C* and *D*). The encapsulated cells and the wild-type cells showed similar illumination intensities within their cell boundaries, likely indicating some dye accumulation on the surface of both types of cells and/or autofluorescence (Fig. 4*E*). Integration of the maximum intensity of scattered light at all illumination angles indicated that the light scattered by the encapsulated cells was significantly more intense than for the wild-type cells (Fig. 4*F*). Analysis of the intensity of scattered light as a function of distance away from the bacterial cells revealed that the light scattered by the encapsulated cells increased in intensity with increasing distance from the cell for the first 2 to 3 µm, then steadily diminished in intensity thereafter (Fig. 4*G*), indicating that the nanojets peaked outside of the encapsulated cells. By contrast, light scattered from wild-type cells showed diminishing intensity with distance from the cells with no clearly defined peak. The intensity of scattered light was more intense for the encapsulated cells than the wild-type cells at every distance from the cells (Fig. 4*G*).

We note that our *E. coli* cells are relatively uniform in width but show more substantial variation in length (*SI Appendix*, Fig. S12 and Table S1). To test whether these variations in length and width would have strong effects on the scattering behavior, for each strain we analyzed equal subpopulations containing the longest 50% of cells and shortest 50% of cells (*SI Appendix*, Fig. S13). The distributions of beam length, beam width, cell intensity, and integrated beam intensity of each subpopulation showed substantial overlap with each other, and only the width of the scattered beams from two strains (TaSil and wild type) showed significant differences in the mean values. We also separated the cells into equal subpopulations containing the widest and narrowest cells from each strain (*SI Appendix*, Fig. S14). We again observed substantial overlap in the distributions of beam statistics. Only the integrated beam intensities of a single strain (SdSil) showed a significant difference in the mean values. These results suggest that the observed variations in cell length and width have minor effects on the scattering behavior.

These data indicate that the polysilicate-encapsulated cells are functioning analogously to dielectric microspheres, creating photonic nanojets that are focused downstream of the cell body. These cells did not show any noticeable degradation in their ability to create photonic nanojets while being measured. Encapsulated cells that had been stored for 6 mo, which no longer showed metabolic activity via alamarBlue assays, still demonstrated scattering of nanojets that were longer, wider, and higher intensity than the 6-mo wild-type cells, with a focal peak several micrometers away from the cells (*SI Appendix*, Fig. S15). A comparison of Fig. 4 and *SI Appendix*, Fig. S15 demonstrates that the nanojets generated by the older cells had slightly reduced intensities compared to the same strains when freshly prepared. These results indicate that polysilicate-encapsulated cells display robust light-focusing ability, which persists for several months postencapsulation, even after the point when the cells cease to be metabolically active.

Encapsulated Cells Are Metabolically Active. To determine the effect of polysilicate encapsulation on bacterial physiology, we evaluated the ability of the encapsulated cells to undergo cell division as well as their metabolic activity. To investigate the

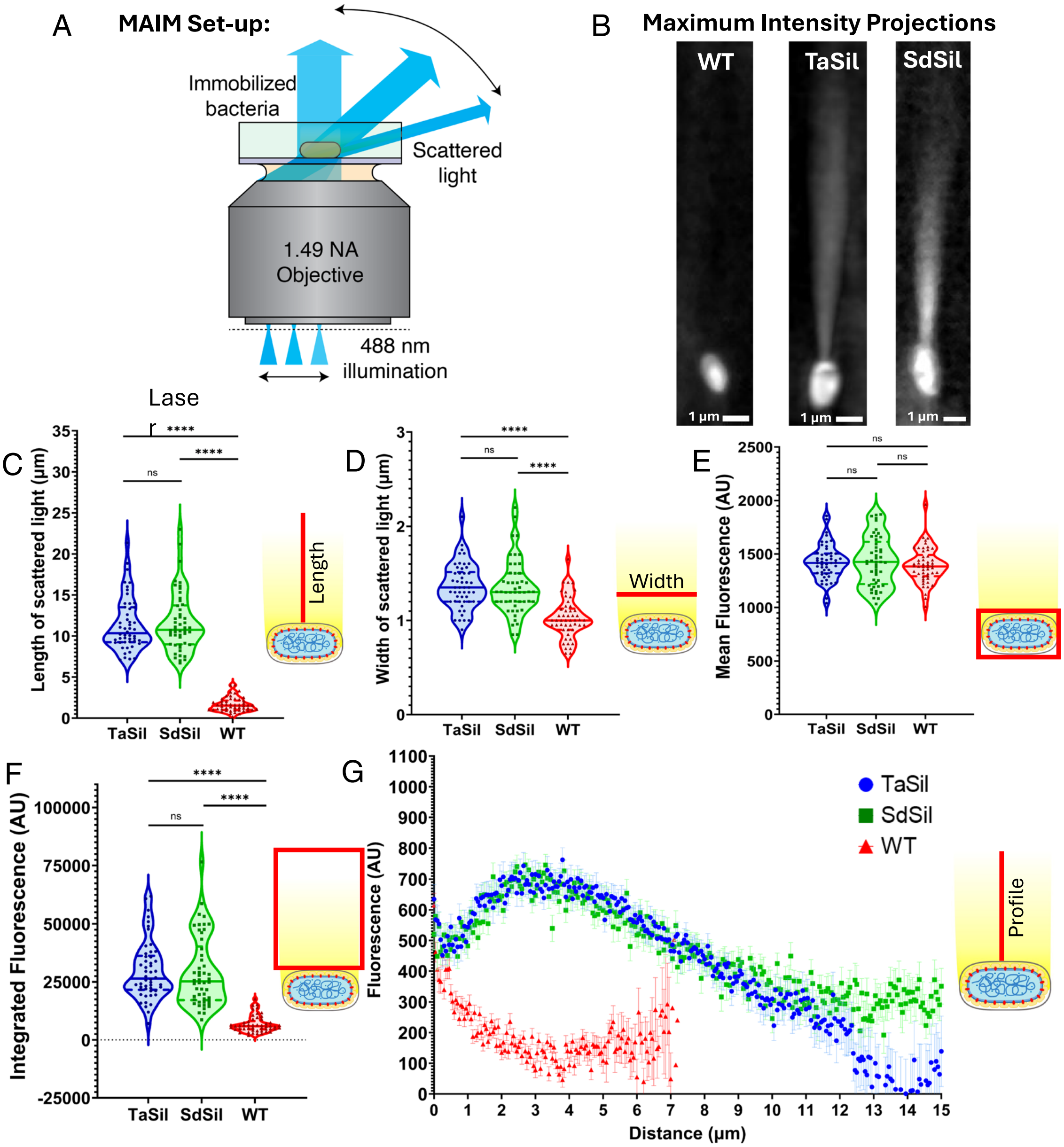

Fig. 4. MAIM indicates that polysilicate-encapsulated cells scatter jets of light that are focused. (*A*) MAIM inverted microscope imaging set-up, allowing visualization of light scattered by bacteria cells at a range of incident angles. (*B*) Maximum intensity projections for silicatein-expressing (TaSil and SdSil) and WT cells scattering light via MAIM. (*C*) Length of scattered light, (*D*) width of scattered light, (*E*) mean intensity of light within cell boundaries, and (*F*) integrated intensity of the scattered light, calculated from maximum intensity projections. (*G*) Intensity of the scattered light as a function of distance from the edge of the cell, calculated from maximum intensity projections. Error bars correspond to SEM. (n = 50) ****$P \leq 0.0001$, ns: not significant.

growth of the silicatein-expressing cells during the induction and encapsulation process, growth curves were measured. Both the TaSil and SdSil strains exhibited slower overall growth compared to wild type, with the TaSil strain approaching zero growth while the SdSil strain showed decreasing cell density, perhaps indicating moderate toxicity of the OmpA-SdSil expression (*SI Appendix*, Fig. S16). Colony sizes were similar to wild-type and consistent across all strains. To determine the effect of polysilicate encapsulation on cell division activity, the strains were induced and incubated with orthosilicate, after which the abilities of the cells to divide were measured via colony-forming unit (CFU) assays. Postencapsulation, the silicatein-expressing strains showed dramatically lower CFU/mL values compared to untreated wild-type cells, with TaSil showing approximately a five-log reduction and SdSil showing approximately a six-log reduction (Fig. 5*A*). Upon storage, the CFUs of all strains steadily diminished over time. CFU/mL values dropped to undetectable levels after 4 mo for the SdSil strain and after 5 mo for the TaSil and wild-type strains. Control samples of TaSil and SdSil strains that were induced but not incubated with orthosilicate showed CFU values over time that were similar to the wild-type strain, as did the EV control strain (*SI Appendix*, Fig. S17*A*). These experiments indicate that the polysilicate-encapsulated cells have predominantly ceased to undergo cell division.

To investigate the effect of polysilicate encapsulation on bacterial metabolic activity, the strains were analyzed using the alamarBlue assay (34), which produces a fluorescent signal upon interaction with the reducing cytoplasmic environment of live, metabolically active cells. Immediately following induction and encapsulation, TaSil and SdSil strains showed alamarBlue activity that was similar to or higher than wild-type cells (Fig. 5*B*). Upon storage, the alamarBlue assay indicated robust intracellular reducing activity for both polysilicate-encapsulated and wild-type cells for several months, until eventually no signal was detected after 4 mo for the SdSil strain or 5 mo for the TaSil and wild-type strains, in agreement with the CFU assays. Silicatein-expressing strains that were induced but not incubated with orthosilicate and EV strains all showed similar alamarBlue activity to the wild-type strain (*SI Appendix*, Fig. S17*B*). These data indicate that polysilicate encapsulation has little effect on the metabolic activity of the bacteria cells and that the encapsulated cells remain metabolically active for several months, despite the massive reduction in cell division.

Discussion

In this work, we demonstrate that microbes can be rationally engineered to improve their ability to focus light into photonic nanojets. We have fused the sea-sponge enzyme silicatein to the outer membrane protein OmpA, directing silicatein to the surface of *E. coli* cells where it can mineralize a polysilicate shell. In agreement with multiphysics simulations, these polysilicate-encapsulated cells are able to scatter an intense beam of light that is focused a short distance downstream from the cell, creating photonic nanojets that are much brighter than wild-type cells. Our self-assembled polysilicate-encapsulated bacteria represent engineered biological microlenses and serve as a proof-of-concept that cells can be engineered to act as tunable photonic components.

Our work builds on previous research using biological approaches for the production of polysilicate materials. Both sea-sponge silicatein enzymes and the silaffin peptide from diatoms have been used to create polymerized silica and silicone materials in vitro (8, 35, 36). *E. coli* bacteria have been modified to express silicatein, both cytoplasmically (7) and on the bacterial surface, and were able to mineralize polysilicate or polylactic acid (37). In a separate study, *E. coli* bacteria were also modified to express recombinant silaffin R5 peptide from diatoms (38, 39), which was able to create silica nanostructures when coexpressed with posttranslational modification enzymes that enhance the biosilification activity of the peptide. Our work demonstrates that engineered bacteria can become encapsulated in a layer of polysilicate, and that this coating enhances the optical properties of the bacteria. Furthermore, this polysilicate-mineralization activity can be implemented by introducing a single enzyme, without requiring additional, exogeneous posttranslational modification enzymes.

Microparticles capable of producing photonic nanojets can be manufactured using nonbiological approaches, but current techniques have several limitations. While microspheres are commercially available using materials such as silica and polystyrene, the spherical geometry is known to produce short nanojets limited to distances close to the particle surface (40). While short and intense nanojets are well suited for some applications, they also make it difficult to couple the nanojets to other devices or to operate them farther away from a surface, limiting their usefulness in other applications. Other geometries, such as microcuboids (41), micropyramids (42), and microdisks (43), have been explored in hopes of producing longer

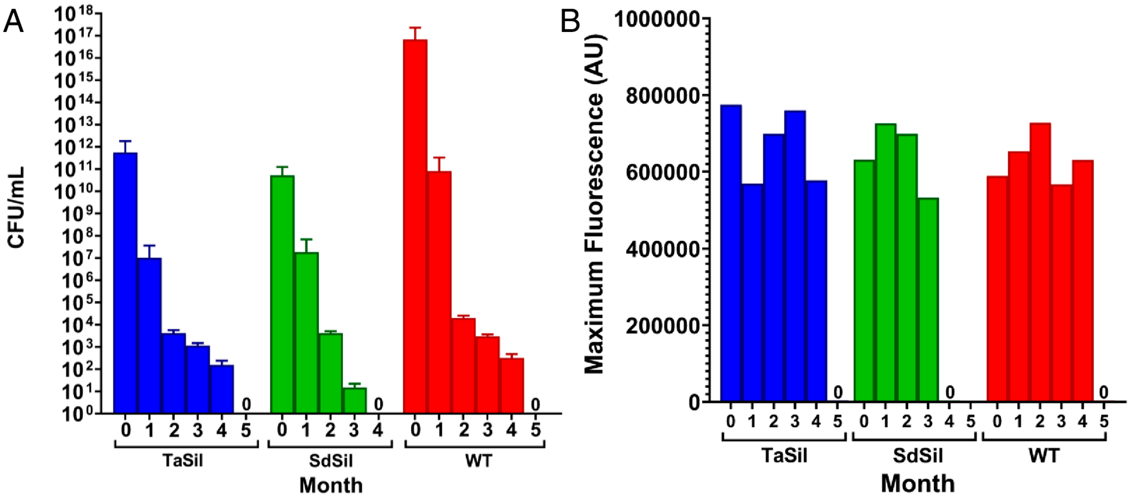

Fig. 5. Reduced cell division and high metabolic activity of encapsulated cells. (*A*) CFU assay results and (*B*) maximum fluorescence values for alamarBlue metabolic activity assays measured for silicatein-expressing (TaSil and SdSil) cells following induction and polysilicate encapsulation and untreated WT cells over 5 mo of storage.

nanojets. Additionally, microspheres with multiple layers have been predicted to produce longer nanojets (44), and microspheres etched with a concentric ring pattern were shown to produce long-working-distance nanojets (45). However, producing these more complicated layered structures has proven challenging and typically requires either low-throughput techniques (45) like focused ion beam etching, toxic chemicals such as hydrofluoric acid (42), or both.

Our approach overcomes several limitations of traditional microparticle manufacturing methods. While spherical microparticles are the easiest to manufacture chemically, bacteria naturally adopt a rod-shaped geometry that is similar to a microcylinder, making them tailored to different applications. Although the length of these cylinders is disperse (~1 to 3 μm), their width is tightly regulated and is maintained to tolerances of approximately 10% (46). We observe that these variations in length and width have relatively modest effects on the size and shape of the nanojets (*SI Appendix*, Figs. S13 and S14), although cell sorting could potentially reduce this variation further. We have shown that we can produce a layered structure by polymerizing a polysilicate shell around our bacteria, and that this layered structure extends the intensity and working distance of the associated photonic nanojets compared to uncoated bacteria. Furthermore, our microparticles do not require expensive specialized equipment to fabricate and are made under ambient conditions without the use of harsh or toxic chemicals. Silicatein-displaying bacteria therefore offer an environmentally friendly, high-throughput path to producing microparticles for use in photonic devices.

While this study is intended as a proof-of-concept demonstration, we can imagine several potential applications for silica-encapsulated bacteria as components in photonic devices. Microlenses have been used to improve the performance of complementary metal oxide semiconductor (CMOS) image sensors, but it has been challenging to design effective microlenses for pixel sizes of 2 μm and below required for high-resolution cameras (47). Polydimethylsiloxane (PDMS) channels have been shown to be capable of capturing bacteria into regular arrays (48), and we envision that a similar approach could be used to place an array of bacteria over a CMOS image sensor (*SI Appendix*, Fig. S18*A*). The small diameter of *E. coli* would mean that such a device could achieve spacings as low as 1 μm. Alternately, encapsulated bacteria could be used to form novel photonic probes for research. Using optical forces from a tapered fiber, Li et al. were able to self-assemble wild-type bacteria into a "nanospear" used for near-field detection (49). Our study suggests that by replacing the wild-type bacteria with encapsulated bacteria, such a device could produce a brighter signal (*SI Appendix*, Fig. S18*B*). A related technique has been used to assemble a waveguide composed of a chain of red blood cells that functions as a biosensor (5). We envision that encapsulated bacteria could be used in place of red blood cells to further miniaturize such a biosensor (*SI Appendix*, Fig. S18*C*).

In addition, the framework we have described here holds great potential for developing additional living microlenses with a range of properties. Our cells have a demonstrated ability to maintain metabolic activity for an extended timeframe of 4 to 5 mo postencapsulation, opening the door to a variety of applications wherein the live biomicrolenses could be used in sense-and-response applications to respond to environmental cues by activating a reporter pathway that would change their optical properties. Additionally, the well-documented ability of the silicatein enzyme to mineralize a range of chemical substrates (6–8, 36–38, 50–54) could allow for the creation of bacteria coated in a variety of materials that will convey unique optical or mechanical properties. Last, bacteria and other microbes can be engineered to grow in an enormous variety of different sizes and shapes, allowing these particles to be tuned to a wide array of applications. In short, living microlenses offer many pathways to engineer new properties for bespoke photonic devices.

Materials and Methods

Modeling of Light Scattering. To simulate the passage of light through the bacteria, the FDTD method was implemented through the use of the commercial software ANSYS Lumerical FDTD: 3D Electromagnetic Simulator. In this method, the simulation region was divided into a fine rectangular grid, and Maxwell's equations were solved within each grid element at each discrete step in time. At one time step, the electric field was calculated, and that solution for the electric field was then used to calculate the magnetic field at the next time step. This process repeated continually, alternating between electric and magnetic field calculations until a steady state was achieved.

Within the simulations, a single bacterial cell was modeled as a rod: a cylinder whose circular faces were each adjoined to a hemisphere of equal diameter. The total length of this structure was 1.8 μm, and the diameter was 0.8 μm. For encapsulated cells, the outer polysilicate layer was modeled to be 30 nm thick by overlaying a second rod concentric with the bacterial cell, with a uniformly larger diameter of 0.86 μm. The refractive indices of the inner rod, outer rod, and surrounding background medium were set to 1.37 (55–57), 1.47, and 1.33, representing cytoplasm, polysilicate, and water, respectively. The cell was positioned centrally along the y- and z-axes, and its long axis was aligned at a variable angle θ to the x-axis. A plane wave of wavelength 488 nm was injected from the leftmost yz-boundary of the simulation region, propagating along the positive x-direction toward the cell. The dimensions of the simulation region were 42 μm × 6 μm × 6 μm, allowing room for the beam of scattered light to be produced. Perfectly matched layer boundary conditions were applied to all boundaries of the simulation region.

Simulations were performed separately for encapsulated cells and wild-type cells, for values of θ ranging from 0° to 90° in increments of 5°. The inclusion of a range of θ values models the random orientation of cells within the experimental methodology. Cells were rotated instead of the entire modeled boundary to limit the computing power needed to achieve the same simulated results and keep analysis streamlined across all cell angles.

Analysis of Modeling Data. A 2-dimensional intensity map was produced from the steady-state solution by summing the electric field intensity values along the range of z-values spanned by the bacterial cell. The background intensity value for each intensity map was calculated from the mean intensity of the lower-left corner square region comprising an area of 1 μm^2, close to the light source and unaffected by the interactions between the light source and the cell. The beam region was defined as all points within the intensity map whose x-values were beyond the right edge of the cell, for which the intensity values were at least 30% greater than the background intensity value, and which were part of a contiguous set of points in the central y-region. The width of the beam was measured as the greatest difference in y-values between any two points with matching x-values along the perimeter of the beam region. The length of the beam was measured by subtracting the x-position of the right edge of the cell from the x-position of the furthest-right point within the beam region. A map of background-adjusted intensity values was produced by subtracting the background intensity value from all points within the intensity map, and any resulting negative intensity values were set to a value of 0. The intensity values were then normalized by applying the equation: $\frac{\text{Intensity}}{\text{Highest intensity across all simulations}}$. The integrated intensity of the beam was calculated by summing all intensity values within the beam region. The profile of the beam was determined by measuring the background-adjusted intensity as a function of the distance from the right edge of the cell along the centerline of the beam, defined as the subcollection of points within the beam region whose y-values were 0. To calculate the FWHM, the transverse beam profile was generated by identifying the z-position of the maximum intensity within the 3-dimensional simulation region, extracting the xy-plane of intensity values at that z-position, and measuring the intensity along the y-direction at the x-position of the maximum intensity point. The FWHM of the beam was measured as the width of the peak of the transverse beam profile at the intensity value halfway between the maximum intensity and the background intensity value of the corresponding xy-plane.

In order to approximate the effect of imaging the excitation pattern produced by the nanojet on a widefield fluorescent microscope, we convolved the results of the multiphysics model with a Gaussian approximation to the point spread function (58). The wavelength was estimated as 517 nm, corresponding to the emission peak of the Alexa Fluor 488 dye. The NA of the objective was set to 1.49.

Strain Information. The strain background used for all experiments is Top10 *E. coli* [genotype: F- mcrA Δ(mrr-hsdRMS-mcrBC) φ80lacZΔM15 ΔlacX74 recA1 araD139 Δ(araleu) 7697 galU galK rpsL (StrR) endA1 nupG)], which is a nonmotile laboratory strain. cDNA encoding silicatein genes from two species of sea sponges, *T. aurantia* (22) (GenBank: AF032117.1) and *S. domuncula* (20, 22) (GenBank: AJ272013.1), was *E. coli* codon-optimized and used to construct silicatein-expressing plasmids. OmpA-silicatein constructs were created by fusing the signaling peptide and the first nine N-terminal amino acids of lipoprotein Lpp from *E. coli*; amino acids 46 to 159 of OmpA which form its transmembrane domain (28); and silicatein complementary DNA. The plasmid containing the OmpA-TaSil fusion protein contains a strong ribosome binding site [B0034 (59, 60)] upstream of the TaSil fusion protein and the rrnB T1 and T7Te terminators. OmpA-TaSil silicatein was inserted into vector pBbS5a-RFP (61) (Addgene #35283) replacing the vector's RFP gene, placing TaSil expression under the control of an inducible Lac promoter (62). The OmpA-SdSil fusion protein was placed behind RBS (B0034) and cloned into the pRHA113 vector's multiple cloning site using XbaI and BamHI, placing the SdSil gene under an inducible rhamnose promoter. The pRHA113 OmpA-SdSil construct needs to be retransformed periodically into *E. coli*, as the silicatein expression becomes more variable with longer storage at −80 °C. The EV control in the paper refers to the background strain containing the pRHA113 vector backbone with no gene insertion, and wild type (WT) refers to the background strain containing no plasmid.

Culture Growth Conditions. An overnight culture was prepared for each strain, via growth at 37 °C in Luria-Bertani (LB) media on a rotator. After overnight growth, a fresh culture was inoculated via a 1/100 dilution of overnight culture into fresh LB media, with 100 μg/mL final concentration of ampicillin for TaSil, SdSil, and EV strains, in liquid suspension in an Erlenmeyer flask. Cells were grown for 2 h at 37 °C with shaking at 250 rpm. The modified strains grew at a similar rate to wild-type cells (*SI Appendix*, Fig. S16). Silicatein expression was induced by adding isopropyl ß-D-1-thiogalactopyranoside (IPTG; CAS: 367-93-1) to 1 mM final concentration for the TaSil strain or rhamnose (Sigma Aldrich, CAS: 10030-85-0) to 0.2% final concentration for SdSil and pRHA113 EV strains. Cells were induced for 3 h at 37 °C with shaking, and then sodium orthosilicate (Na_4SiO_4, Alfa Aesar, CAS: 13472-30-5) was added to a final concentration of 100 μM. Cells were incubated with silicate for 3 h at 37 °C with shaking at 250 rpm. Cells were then pelleted at 4,500 rpm for 10 min in a swinging bucket centrifuge, and excess silicate was removed by washing three times with 1× Tris buffered saline (TBS: 50 mM Tris-HCl, 150 mM NaCl, pH 7.5). Finally, cells were resuspended in 1× TBS and stored at 4 °C with constant rotation (Benchmark Scientific Roto-Mini Plus Variable Speed Rotator R2024) at 30 rpm until use.

Cell Fixation for Immunofluorescence. After growth and incubation with inducer chemicals and sodium orthosilicate, cells were fixed in 2.5% glutaraldehyde in 1× phosphate-buffered saline (PBS–MP Biomedicals, CAS: 2810306) for 1.5 h at room temperature. Cells were washed three times with 1× PBS and resuspended in 1× PBS. Fixed cells were stored in 1× PBS at 4 °C with constant rotation until use in immunofluorescence.

Immunofluorescence. Fixed cells were blocked with 2% Bovine Serum Albumin (BSA) in 1× PBS for 10 min at room temperature. Primary antibody (Silicatein alpha/silica-G antibody, Antibodies-online, ABIN191460) was added at a 1:100 dilution to the 2% BSA-cell solution. Cells were incubated with primary antibody overnight at 4 °C with constant rotation. Next, cells were washed three times with 1× PBS and then incubated with the secondary antibody (Goat Anti-Rabbit IgG H&L, Alexa Fluor® 647, Abcam, ab150079) at a 1:500 dilution in 2% BSA in 1× PBS for 1 h at room temperature in the dark. Cells were then washed three times with 1× PBS and prepped for imaging via resuspension in VectaShield® Antifade mounting medium with DAPI (Vector Laboratories UX-93952-24). Cells were pipetted onto a 1% agarose pad and sealed with a coverslip for imaging on a Nikon A1R HD Laser Scanning Confocal Microscope using a 60× oil Apochromat Total internal reflection fluorescence (TIRF) objective (1.49 NA). DAPI staining of DNA was imaged using a 405 nm excitation laser and a 425 to 475 nm emission filter, and the secondary antibody was imaged using a 647 nm excitation laser and a 663 to 738 nm emission filter. Images were analyzed using FIJI software (63).

Rhodamine123 Staining. After growth and incubation with inducer chemicals and sodium orthosilicate, live cells were stained with Rhodamine123 (Invitrogen R302) at room temperature and in the dark where possible. 1/10 volume of 500 μM Rhodamine123 was added to the bacteria culture (i.e., 1 μL Rhodamine123 for every 10 μL culture), followed by a 15-min incubation. Cells were washed three times with 1× TBS, then resuspended in 1× TBS. Cells were pipetted onto a 1% agarose pad and sealed with a coverslip for imaging on a Nikon A1R HD Laser Scanning Confocal Microscope using a 60× oil Apochromat TIRF objective (1.49 NA). Rhodamine123 signal was imaged using a 488 nm excitation laser and a 500 to 550 nm emission filter. Images were analyzed using FIJI software.

Cell Preparation for TEM. After growth and incubation with inducer chemicals and sodium orthosilicate, cells were fixed in a solution of 2.5% glutaraldehyde in 0.1 M sodium cacodylate buffer overnight at 4 °C with constant rotation. Cells were spun down and rinsed twice for 10 min in the same fixation buffer. The postfixation samples were resuspended in 1% osmium tetroxide and incubated for 30 min. Cells were spun down and rinsed twice for 10 min in dH$_2$O, and the supernatant was removed from the pelleted cells. Cells were trapped in 3% agarose, which was cut into 1 mm cubes. The cubes were dehydrated in a graded ethanol series (50%, 65%, 80%, 95%, 100%) three times for 20 min at each step. Samples were transferred into propylene oxide:ethanol [1:1] and incubated for 30 min, then incubated twice for 30 min in 100% propylene oxide. Samples were incubated in epoxy resin:propylene oxide [1:1] with rotation for 2.5 h, then incubated in 100% epoxy resin overnight. Samples were embedded into molds and polymerized at 65 °C for 48 h. Cells were cut using a Leica UC7 ultramicrotome, on a diamond knife, into 1-micron sections. The sections were stained on a glass slide with Toluidine blue and rinsed with dH$_2$O. Sections were selected for thin sectioning via light microscopy, cut to 70 nm sections, and placed onto formvar/carbon nickel slot grids (Electron Microscopy Sciences, Hatfield, PA). Grids were stained with aqueous 2% uranyl acetate and 3% lead citrate. Cells were imaged on a Hitachi 7650 Transmission Electron Microscope at 80 kV with an attached Gatan Erlangshen 11-megapixel digital camera.

Cell Surface Roughness Calculations. Using FIJI, individual cells were isolated from the TEM micrographs, and the cell images were duplicated. For each cell analyzed, a 2-pixel Gaussian blur was performed on one duplicate, and a 10-pixel Gaussian blur was performed on the other. The outer edge of the cell was outlined using the lasso tool, and the perimeter was measured for both blurred images. Cell surface roughness was calculated as $\text{Perimeter}_{(\text{Blur2})} - \text{Perimeter}_{(\text{Blur10})}$.

SEM-EDS Analysis. Samples stored in 1× TBS buffer were centrifuged, pelleted, and washed twice with distilled water. Each sample was resuspended in approximately 1 mL of distilled water to achieve a homogenous mixture. To prepare for SEM-EDS analysis, 50 to 60 μL of each sample was deposited onto an SEM sample holder and allowed to dry overnight. The samples were sputter coated with a 3 nm layer of platinum. SEM imaging was performed on a Hitachi SU3500 in secondary electron mode at an accelerating voltage of 10 keV and a working distance of 5 mm. EDS analysis was performed with an accelerating voltage of 15 keV and a working distance of 10 mm.

X-Ray Powder Diffraction (XRD) Analysis. Samples stored in 1× TBS buffer were centrifuged, pelleted, and washed twice with distilled water. Each sample was resuspended in approximately 1 mL of distilled water to achieve a homogenous mixture. To prepare for XRD analysis, 150 μL of each sample was deposited onto an XRD sample holder with a zero-diffraction plate and allowed to dry overnight. Mineral phases of each bacterial sample were analyzed qualitatively using a Bruker D8 Advance XRD system. Cu Kα X-ray radiation with wavelength 1.5406 Å was used to scan from 10° to 60° 2θ with a step size of 0.02° and a dwell time of 1 s per step.

Optical Trapping of Encapsulated Cells. Bacterial cells were flowed into a LUMICKS C-trap microscope equipped with optical tweezers. Bacteria were captured into an optical trap and calibrated using a two-step process. First, the stage was swept in a sinusoidal pattern to displace the bead from center of the trap. This motion was captured both by video tracking and by using the voltage signal on the quadrant photodiode, and by comparing these two records we could accurately determine the voltage-to-displacement relationship. The Brownian motion of the bacteria was then recorded with the stage held fixed and was used to generate a power spectrum. The power spectrum was fit to the functional form expected from a spherical particle (32). This allowed us to extract both the diffusion coefficient and the trap stiffness for each particle. The diffusion coefficient was then used to calculate an equivalent spherical diameter as a rough estimate of the size of the bacterium. The stiffness was then fit as a linear function of the equivalent diameter ($y = m*x$), and the slopes were compared for bacteria from each strain. To verify this validity of this technique, we trapped polystyrene and silica beads with nominal diameters of 1.4 μm and refractive indices at the trapping wavelength of 1.57 and 1.45, respectively, and analyzed them the same way.

To estimate the significance of the observed differences in the slope of stiffness vs. diameter, a bootstrap analysis was performed. Pairs of datasets were first combined to estimate a null distribution. Equal amounts of cells were randomly drawn with replacement from this null distribution and fit to a linear function. The fraction of times the slopes extracted from these simulated experiments differed by more than the measured difference was used to estimate the *P*-value.

Microscope Setup. A custom-built microscope was used to perform MAIM. Three lasers (488 nm, 532 nm, and 640 nm) were combined into an acousto-optic modulator (Brimrose) and coupled into a single mode fiber. The other end of the fiber was coupled to a beam expander followed by a focusing lens. These three components (fiber coupler, beam expander, and focusing lens) were all placed on a motorized translation stage (Thorlabs). The laser illumination was then reflected off a dichroic beam splitter (Chroma), allowing the beam to come to a focus at the back focal plane of a 100X 1.49 NA oil immersion objective (Nikon), producing uniform, planar illumination at the image plane. Adjusting the motorized translation stage allowed us to continuously change the angle of illumination at the image plane. Transmitted light from an light emitting diode (Thorlabs) along with fluorescence emitted in the image plane was collected by the objective and passed through the dichroic beam splitter to a tube lens (Thorlabs). The tube lens focused the light through a second dichroic beam splitter, which separated the fluorescent emission from the transmitted light emitting diode illumination onto two scientific complementary metal-oxide-semiconductor cameras (Thorlabs). This setup allowed us to image both the bacteria in brightfield and the fluorescent patterns caused by the 488 nm laser light scattered by the bacteria.

MAIM. An agarose pad was prepared for imaging by melting 1% agarose in a 0.01% poly-lysine solution and solidifying it into the desired pad shape (7/16 diameter circle, 0.5 mm thick, approximately 100 μL volume). Once solidified, the pad was placed in a dark humidity chamber and stained for 20 min with 20 μL of 0.5 mg/mL Alexa Fluor™ 488 NHS Ester (Invitrogen A20000) dissolved in a solution of 0.1 M sodium bicarbonate pH 8.3. Excess succinimidyl ester was quenched with a 1 M glycine rinse over the pad. Cells were then pipetted onto the fluorescently stained agarose pad and sealed with a coverslip. The cells were imaged using a custom-built inverted fluorescence microscope. Laser illumination at 488 nm was delivered to the 100× oil-immersion objective (Nikon, 1.49 NA) through a fiber launcher and telescope placed on a motorized translation stage, allowing smooth variation of the illumination angle from total internal reflection at the glass–water interface to any angle between −90˚ and 90˚ above the coverslip (where 0˚ corresponds to epi-illumination). A low laser intensity was chosen (200 μW total, ~0.005 μW/μm^2 in the image plane) to minimize photodamage and bleaching of the dyes. Fluorescent images were acquired for multiple illumination angles spanning the full range of angles.

MAIM Image Processing. MAIM images were processed using FIJI. A rolling ball background subtraction (50-pixel radius) was performed on all images and movies, then a maximum intensity Z projection was created from each movie. The maximum intensity images were used for performing image analysis including length, width, integrated fluorescence, mean fluorescence of light within the cell boundary, and profile of scattered light. The jet was defined as a contiguous region downstream of the bacterial cells for which the intensity values were greater than the background intensity value. The length of the jet was defined as the length of a line drawn from the edge of the cell through the center of the jet of light to the distal edge of the jet. The width was defined as the widest point of the jet beam, measured perpendicularly to the angle of incident light. The integrated fluorescence of the jet of scattered light was calculated by creating the smallest box that included the entire jet and measuring the integrated density within the area of the box. The mean fluorescence of light within the cell boundary was measured by drawing a box around only the bacterial cell and calculating the mean gray value within the box. The profile of scattered light was determined by drawing a single line through the center of the jet of light beginning at the cell edge and continuing to the first location that matched the background level of fluorescence, then obtaining the profile using the plot profile function of imageJ. The background level of fluorescence for each maximum intensity image was subtracted from the scattered light profiles.

Cell Length and Width Analyses. The same cells used for the MAIM analysis were also measured to determine their lengths and widths. Using FIJI, a line was drawn lengthwise, determined as the longest axis of the cell, and a line was drawn widthwise, determined as the shorter axis of the cell. The cells were then binned into above or below the average for each strain (TaSil, SdSil, WT) to determine whether the dimensions of the cells had an impact on the MAIM results.

Growth Curves. Cells were cultured as described above, with the exception that cultures were grown in a 96-well plate. The plate was incubated at 37 °C with continuous orbital shaking at 282 rpm in a microplate reader (BioTek Synergy H1), which recorded OD_{600} measurements every 15 min for a total of 8.5 h, with breaks for the addition of the inducer chemical and sodium orthosilicate.

CFU Assay. Cells were resuspended to an OD_{600} of 0.1 in LB (with antibiotics) and were serially diluted in 1× TBS. 100 μL of the diluted cells were plated onto appropriate media for each condition (LB for WT, LB+ampicillin for plasmid-containing strains). Plates were incubated overnight at 37 °C, and colonies were counted the following morning. The following equation was used to calculate the CFU/mL of the samples: $\frac{\#\ of\ Colonies*Dilution\ factor}{Volume\ of\ cells\ plated}$.

AlamarBlue Cell Viability Assay. After growth and incubation with inducer chemicals and sodium orthosilicate, cells were resuspended to an OD_{600} of 0.1 in LB (with antibiotics). The cells were diluted to 10^{-1} in 1× TBS. Two 100 μL aliquots of each sample were loaded into a black, clear bottom 96-well plate. Half of the samples were monitored for alamarBlue fluorescence (Ex: 530 nm/Em: 590 nm) and the other half for absorbance at 600 nm to determine a growth curve, since the absorbance spectrum of alamarBlue overlaps with the OD_{600} measurements used to determine growth curves. 10 μL of alamarBlue (Invitrogen DAL1025) was added to the samples that were monitored for fluorescence. Each sample and dilution were analyzed in triplicate. A BioTek Synergy H1 microplate reader was used to incubate and continuously orbital shake (282 rpm) the 96-well plate at 37 °C. Readings were taken every 15 min for 24 h. 1× TBS samples were used as negative controls for the alamarBlue assays, and LB samples were used as negative controls for the cell growth curves. Fluorescence or OD_{600} values of negative control samples were subtracted from each experimental dataset to correct for background signal.

Statistical Analyses. Wilcoxon *t* tests were performed using GraphPad Prism version 9.1.0 for Windows, GraphPad Software, San Diego, California USA for all statistical analyses.

Data, Materials, and Software Availability. All study data are included in the article and/or supporting information.

ACKNOWLEDGMENTS. We wish to thank Delft University of Technology's 2016 International Genetically Engineered Machine (iGEM) team for the initial development and work done on this project: Carmen Berends, Célina Reuvers, Charlotte Koster, Giannis Papazoglou, Iris de Vries, Lara van der Woude, Liza de Wilde, and Tessa Vergroesen; Filipe Natalio for initial discussions; Matthew Hamilton Fyfe from University of Colorado Boulder for assistance with elemental analyses laboratory support in Wil V. Srubar III's laboratory; Morgan Brady from the University of Rochester for laboratory and project development and suggestions; Karen Bentley, Chad Galloway, and Kelsea Cristillo of the Electron Microscopy Resource in the Center for Advanced Research Technologies at the University of Rochester Medical Center for performing electron microscopy imaging; the University of Rochester Medical Center's Center for Advanced Light Microscopy and Nanoscopy, especially Julie Zhang and Kaye Thomas for their assistance with confocal microscopy; Brian McIntyre and Sean O'Neil from the University of Rochester's Integrated Nanosystems Center for electron microscopy imaging and technique guidance. Funding to L.M.S., M.M.B., E.A.A., and A.S.M. was provided by the NSF via MODULUS DSM-2031180, ITE-2137561, and ITE-2230641, and by the NIH via 1R01GM143182-01. L.M.S. was supported in part by a fellowship award under contract FA9550-21-F-0003 through the National Defense Science and Engineering Graduate Fellowship Program, sponsored by the Air Force Research Laboratory, the Office of Naval Research and the Army Research Office. I.R. and P.S.C. were funded by the University of Rochester. Funding for B.C.A., J.R., and W.V.S. was provided by the NSF via CMMI-1943554. Optical tweezer measurements by E.J and E.A.A. were funded by the NIH via 1S10OD030296-01A1.

Author affiliations: [a]Department of Biology, University of Rochester, Rochester, NY 14627; [b]Department of Physics and Astronomy, University of Rochester, Rochester, NY 14627; [c]Institute of Optics, University of Rochester, Rochester, NY 14627; [d]Department of Civil, Environmental, and Architectural Engineering, University of Colorado Boulder, Boulder, CO 80309; [e]Department of Biotechnology, Delft University of Technology, Delft 2629 HZ, The Netherlands; and [f]Materials Science and Engineering Program, University of Colorado Boulder, Boulder, CO 80309

1. Y. C. Li, X. S. Liu, B. J. Li, Single-cell biomagnifier for optical nanoscopes and nanotweezers. *Light Sci. Appl.* **8**, 61 (2019).
2. Y. C. Li, X. Liu, H. Lei, Y. Zhang, B. Li, Enhancing upconversion fluorescence with a natural bio-microlens. *ACS Nano* **11**, 10672–10680 (2017).
3. N. Schuergers *et al.*, Cyanobacteria use micro-optics to sense light direction. *Elife* **5**, 12620 (2016).
4. E. De Tommasi *et al.*, Biologically enabled sub-diffractive focusing. *Opt. Express* **22**, 27214–27227 (2014).
5. Y. Li *et al.*, Red-blood-cell waveguide as a living biosensor and micromotor. *Adv. Funct. Mater.* **29**, 1905568 (2019).
6. X. Li, Z. Chen, A. Taflove, V. Backman, Optical analysis of nanoparticles via enhanced backscattering facilitated by 3-D photonic nanojets. *Opt. Express* **13**, 526–533 (2005).
7. Z. Chen, A. Taflove, V. Backman, Photonic nanojet enhancement of backscattering of light by nanoparticles: A potential novel visible-light ultramicroscopy technique. *Opt. Express* **12**, 1214–1220 (2004).
8. J. Zhu, L. L. Goddard, All-dielectric concentration of electromagnetic fields at nanoscale: The role of photonic nanojets. *Nanoscale Adv.* **1**, 4615–4643 (2019).
9. A. Darafsheh, Photonic nanojets and their applications. *J. Phys. Photonics* **3**, 022001 (2021).
10. A. V. Itagi, W. A. Challener, Optics of photonics nanojets. *J. Opt. Soc. Am.* **22**, 2847–2858 (2005).
11. S. Lecler, Y. Takakura, P. Meyrueis, Properties of a three-dimensional phonic nanojet. *Opt. Lett.* **30**, 2641–2643 (2005).
12. X. Mao *et al.*, Tunable photonic nanojet formed by generalized Luneburg lens. *Opt. Express* **23**, 26426–26433 (2015).
13. S. Yang *et al.*, Functional biomimetic microlens arrays with integrated pores. *Adv. Mater.* **17**, 435–438 (2005).
14. J. Aizenberg, A. Tkachenko, S. Weiner, L. Addadi, G. Hendler, Calcitic microlenses as part of the photoreceptor system in brittlestars. *Nature* **412**, 4 (2001).
15. J. Aizenberg, G. Hendler, Designing efficient microlens arrays: Lessons from nature. *J. Mater. Chem.* **14**, 2066–2072 (2004).
16. V. C. Sundar, A. D. Yablon, J. L. Grazul, M. Ilan, J. Aizenberg, Fibre-optical features of a glass sponge. *Nature* **424**, 899–900 (2003).
17. K. Shimizu, J. Cha, G. D. Stucky, D. E. Morse, Silicatein: Cathepsin L-like protein in sponge biosilica. *Proc. Natl. Acad. Sci. U.S.A.* **95**, 6234–6238 (1998).
18. K. Shimizu, D. E. Morse, "Silicatein: A unique silica-synthesizing catalytic triad hydrolase from marine sponge skeletons and its multiple applications" in *Methods in Enzymology* (Elsevier, 2018), **vol. 605**, pp. 429–455.
19. J. N. Cha *et al.*, Silicatein filaments and subunits from a marine sponge direct the polymerization of silica and silicones in vitro. *Proc. Natl. Acad. Sci. U.S.A.* **96**, 361–365 (1999).
20. W. E. G. Müller *et al.*, Siliceous spicules in marine demosponges (example Suberites domuncula). *Micron Oxf. Engl.* **37**, 107–120 (2006).
21. W. E. G. Müller *et al.*, Formation of siliceous spicules in the marine demosponge Suberites domuncula. *Cell Tissue Res.* **321**, 285–297 (2005).
22. W. Muller *et al.*, Bioencapsulation of living bacteria (Escherichia coli) with poly(silicate) after transformation with silicatein-α gene. *Biomaterials* **29**, 771–779 (2008).
23. W. E. G. Müller *et al.*, Poly(silicate)-metabilizing silicatein in siliceous spicules and silicasomes of demosponges comprises dual enzymatic activities (silica polymerase and silica esterase). *FEBS J.* **275**, 362–370 (2007).
24. F. Natalio *et al.*, Bioengineering of the silica-polymerizing enzyme silicatein-α for a targeted application to hydroxyapatite. *Acta Biomater.* **6**, 3620–3728 (2010).
25. Y. J. Wang, C. A. Dai, J. H. Li, Numerical study of tunable photonic nanojets generated by biocompatible hydrogel core-shell microspheres for surface-enhanced Raman scattering applications. *Polymers* **11**, 431 (2019).
26. A. Mandal, V. R. Dantham, Short and elongated photonic nanojets emerged from single solid/hollow core-shell microparticles illuminated by focused Gaussian beams and plane wave. *J. Quant. Spectrosc. Radiat. Transf.* **257,** 107350 (2020).
27. P. Anger, P. Bharadwaj, L. Novotny, Enhancement and quenching of single-molecule fluorescence. *Phys. Rev. Lett.* **96**, 113002 (2006).
28. J. A. Francisco, C. F. Earhart, G. Georgiou, Transport and anchoring of beta-lactamase to the external surface of Escherichia coli. *Proc. Natl. Acad. Sci. U.S.A.* **89**, 2713–2717 (1992).
29. E.-J. Kim, S.-K. Yoo, Cell surface display of CD8 ecto domain on Escherichia coli using ice nucleation protein. *Biotechnol. Tech.* **12**, 197–201 (1998).
30. Z. Darzynkiewicz, F. Traganos, L. Staiano-Coico, J. Kapuscinski, M. R. Melamed, Interaction of rhodamine 123 with living cells studied by flow cytometry. *Cancer Res.* **42**, 799–806 (1982).
31. H. T. Nguyen *et al.*, Comparison of two transmission electron microscopy methods to visualize drug-induced alterations of Gram-negative bacterial morphology. *Antibiotics* **10**, 307 (2021).
32. K. Berg-Sorensens, H. Flyvbjerg, Power spectrum analysis for optical tweezers. *Rev. Sci. Instrum.* **75**, 594–612 (2004).
33. N. Wang, X. Li, J. Chen, Z. Lin, J. Ng, Gradient and scattering forces of anti-reflection-coated spheres in an aplanatic beam. *Sci. Rep.* **8**, 17423 (2018).
34. S. N. Rampersad, Multiple applications of Alamar Blue as an indicator of metabolic function and cellular health in cell viability bioassays. *Sensors* **12**, 12347–12360 (2012).
35. H. C. Schröder *et al.*, Acquisition of structure-guiding and structure-forming properties during maturation from the pro-silicatein to the silicatein form. *J. Biol. Chem.* **287**, 22196–22205 (2012).
36. R. Wieneke *et al.*, Silica precipitation with synthetic silaffin peptides. *Org. Biomol. Chem.* **9**, 5482–5486 (2011).
37. P. Curnow, D. Kisailus, D. E. Morse, Biocatalytic synthesis of poly(L-lactide) by native and recombinant forms of the silicatein enzymes. *Angew. Chem. Int. Ed. Engl.* **45**, 613–616 (2006).
38. A. K. Wallace, N. Chanut, C. A. Voigt, Silica nanostructures produced using diatom peptides with designed post-translational modifications. *Adv. Funct. Mater.* **30**, 2000849 (2020).
39. B. M. Kırpat Konak *et al.*, A living material platform for the biomineralization of biosilica. *Mater. Today Bio* **17**, 100461 (2022).
40. S. Surdo, M. Duocastella, A. Diaspro, Nanopatterning with photonic nanojets: Review and perspectives in biomedical research. *Micromachines* **12**, 256 (2021).
41. C. Y. Liu, Photonic jet produced by dielectric micro cuboids. *Appl. Opt.* **54**, 8694–8699 (2015).
42. J. Martin, J. Proust, D. Gérard, J. L. Bijeon, J. Plain, Intense Bessel-like beams arising from pyramid-shaped microtips. *Opt. Lett.* **37**, 1274–1276 (2012).
43. A. McGloskey, J. J. Wang, J. F. Donegan, Low divergence photonic nanojets from Si3N4 microdisks. *Opt. Express* **20**, 128–140 (2012).
44. Y. Shen, L. V. Wang, J. T. Shen, Ultralong photonic nanojet formed by a two-layer dielectric microsphere. *Opt. Lett.* **39**, 4120–4123 (2014).
45. M. X. Wu *et al.*, Modulation of photonic nanojets generated by microspheres decorated with concentric rings. *Opt. Express* **23**, 20096–20103 (2015).
46. L. Furchtgott, N. S. Wingreen, K. C. Huang, Mechanisms for maintaining cell shape in rod-shaped Gram-negative bacteria. *Mol. Microbiol.* **81**, 340–353 (2011).
47. Y. Huo, C. C. Fesenmaier, P. B. Catrysse, Microlens performance limits in sub-2μm pixel CMOS image sensors. *Opt. Express* **18**, 5861–5872 (2010).
48. P. Wang *et al.*, Robust growth of Escherichia coli. *Curr. Biol.* **20**, 1099–1103 (2010).
49. Y. Li *et al.*, Living nanospear for near-field optical probing. *ACS Nano* **12**, 10703–10711 (2018).
50. F. Natalio *et al.*, Silicatein-mediated incorporation of titanium into spicules from the demosponge Suberites domuncula. *Cell Tissue Res.* **339**, 429–436 (2010).
51. R. L. Brutchey, D. E. Morse, Silicatein and the translation of its molecular mechanism of biosilicification into low temperature nanomaterial synthesis. *Chem. Rev.* **108**, 4915–4934 (2008).
52. P. Curnow *et al.*, Enzymatic synthesis of layered titanium phosphates at low temperature and neutral pH by cell-surface display of silicatein-α. *J. Am. Chem. Soc.* **127**, 15749–15755 (2005).
53. M. N. Tahir *et al.*, Formation of layered titania and zirconia catalysed by surface-bound silicatein. *Chem. Commun.* **44**, 5533–5535 (2005).
54. N. V. Povarova *et al.*, Efficient silica synthesis from tetra(glycerol)orthosilicate with cathepsin- and silicatein-like proteins. *Sci. Rep.* **8**, 16759 (2018).
55. X. J. Liang, A. Q. Liu, C. S. Lim, T. C. Ayi, P. H. Yap, Determining refractive index of single living cell using an integrated microchip. *Sens. Actuators A Phys.* **113**, 349–354 (2007).
56. A. E. Balaev, K. N. Dvoretski, V. A. Doubrovski, Refractive index of Escherichia coli cells. *SPIE* **4707**, 253–360 (2002).
57. B. Zhang, J. Zerubia, J. C. Olivo-Marin, Gaussian approximations of fluorescence microscope point-spread function models. *Appl. Opt.* **46**, 1819–1829 (2007).
58. W. Choi *et al.*, Tomographic phase microscopy. *Nat. Methods* **9**, 717–719 (2007).
59. M. B. Elowitz, M. G. Surette, P.-E. Wolf, J. B. Stock, S. Leibler, Protein mobility in the cytoplasm of Escherichia coli. *J. Bacteriol.* **181**, 197–203 (1999).
60. V. S. Mahajan *et al.*, Part:BBa_B0034. iGEM Registry of Standard Biological Parts. https://parts.igem.org/wiki/index.php/Part:BBa_B0034. Accessed 21 November 2024.
61. T. S. Lee *et al.*, BglBrick vectors and datasheets: A synthetic biology platform for gene expression. *J. Biol. Eng.* **5**, 12 (2011).
62. L. Kamoen, M. Vazquez, Part:BBa_K1890002. iGEM Registry of Standard Biological Parts. https://parts.igem.org/wiki/index.php/Part:BBa_K1890002. Accessed 21 November 2024.
63. J. Schindelin *et al.*, Fiji: An open-source platform for biological-image analysis. *Nat. Methods* **9**, 676–682 (2012).